Magnetic Resonance Imaging of Water Freezing in Packed Beds Cooled from Below

J. G. Georgiadis and M. Ramaswamy

ACRC TR-88 October 1995

For additional information:

Air Conditioning and Refrigeration Center
University of Illinois
Mechanical & Industrial Engineering Dept.
1206 West Green Street
Urbana, IL 61801

(217) 333-3115

Prepared as part of ACRC Project 58
Frost Growth on Conventional, Coated,
and Enhanced Heat Transfer Surfaces
J. G. Georgiadis and A. M. Jacobi, Principal Investigators

The Air Conditioning and Refrigeration Center was founded in 1988 with a grant from the estate of Richard W. Kritzer, the founder of Peerless of America Inc. A State of Illinois Technology Challenge Grant helped build the laboratory facilities. The ACRC receives continuing support from the Richard W. Kritzer Endowment and the National Science Foundation. The following organizations have also become sponsors of the Center.

Acustar Division of Chrysler
Amana Refrigeration, Inc.
Brazeway, Inc.
Carrier Corporation
Caterpillar, Inc.
Delphi Harrison Thermal Systems
Eaton Corporation
Electric Power Research Institute
Ford Motor Company
Frigidaire Company
General Electric Company
Lennox International, Inc.
Modine Manufacturing Co.
Peerless of America, Inc.
U. S. Army CERL
U. S. Environmental Protection Agency
Whirlpool Corporation

For additional information:

Air Conditioning & Refrigeration Center
Mechanical & Industrial Engineering Dept.
University of Illinois
1206 West Green Street
Urbana IL 61801

217 333 3115

Magnetic Resonance Imaging of water freezing in packed beds cooled from below

John G. Georgiadis and Mahadevan Ramaswamy
Department of Mechanical and Industrial Engineering
University of Illinois at Urbana-Champaign
Urbana, Illinois 61801, USA

ABSTRACT

Full-field quantitative visualization of freezing interfaces requires the introduction of high resolution noninvasive methods. Magnetic Resonance Imaging (MRI) is a versatile tool for mapping the distribution of liquids (primarily water) in three-dimensional space, and is the only practical solution in systems that are strongly refracting or opaque to visible light. MRI is employed to visualize freezing in water-saturated packed beds consisting of spherical beads cooled from below. Imaging of the stagnant interstitial water is accomplished by exploiting the strong contrast in MRI signal between interstitial ice and liquid water. Our implementation of MRI allows fully three-dimensional reconstruction of the solidification front and adequate time resolution to quantify the freezing of the pore water. The wall effect, as expressed by the ratio of bed to bead diameter, is examined with respect to the shape and propagation rate of the freezing interface. MRI can be effective only in media that do not affect the imposed magnetic fields. In heat transfer applications, extra provisions in terms of design and choice of materials of the test section are necessary to accommodate the special environment of the MRI scanner.

NOMENCLATURE

B_0	static magnetic field strength of superconducting MRI scanner [Tesla]
C	specific heat [J kg^{-1} K^{-1}]
d	diameter of glass beads [mm]
D	diameter of cylindrical packed bed [mm]
H	height of packed bed [mm]
L	latent heat of fusion [J kg^{-1}]
Ste	Stefan number (dimensionless), $C_{MS}(T_F-T_C)/L$
t	time [sec]
T	temperature [K]
x, y, z	Cartesian coordinates
Z	average distance of ice interface from cooled wall [mm]
Z*	Z/H (dimensionless)

Greek Symbols

α	thermal diffusivity [m^2 sec^{-1}]
ΔT	unwanted temperature rise [K]
κ	thermal conductivity [W m^{-1} K^{-1}]
ρ	density [kg m^{-3}]
τ	dimensionless time, equation (4)
ϕ	porosity
ω_0	Larmor frequency [rad sec^{-1}]

Subscripts

i	initial
C	cold wall
F	ice interface
L	liquid water
LM	liquid water-glass beads mixture
S	ice
SM	ice-glass beads mixture

1. INTRODUCTION

Researchers in the fields of materials processing, fluid mechanics and heat transfer are particularly interested in developments in noninvasive imaging schemes that allow the reconstruction of three-dimensional interfaces and the measurement of growth rates of evolving morphologies. The freezing (or melting) of water occupying the interstitial space of porous materials occurs in a multitude of man-made or natural systems. In applications such as thermal energy storage, natural or artificial freezing of soil, food processing (Hall and Carpenter [1]), and cryosurgery (Hong et al. [2]), information of the shape and evolution of the boundary separating the liquid from the solid (ice) in the pore space is necessary in order to optimize or control the process. A particularly challenging problem arises when there is little or no optical access to the test section, or when the ice mass topology can only be described by volumetric data rather than multiple views (projections).

A standard problem is usually formulated by considering freezing of pore water in fully-saturated packed beds consisting of randomly packed beads contained in a cavity, with one or more walls maintained at a temperature below freezing. The majority of the experimental investigations employ arrays of thermal sensors imbedded in the packed bed, or record the projection of the ice-water interface from a transparent wall, cf. Weaver and Viskanta [3], Chellaiah and Viskanta [4], Yang et al. [5]. The first approach is invasive and gives sparse data from which the mapping of the general interface is impossible. The second gives information about the interface only within a few pore sizes from the transparent wall. Yang et al. [5] examined transient freezing in a square cavity filled with glass or steel beads and water, and suddenly cooled from one side. The cavity side to bead diameter ratio was approximately 10 and the cavity was rotated so that the effect of the cold wall orientation could be studied. Experiments were performed for various orientations and the location of the ice-water interface was inferred by analyzing the area of its projection on the transparent wall. Correlations for the frozen volume as a function of time t were also given: the ice volume grows as $t^{0.62}$ for glass beads and as $t^{0.94}$ for steel beads. An interesting experiment reported by Lein and Tankin [6] exploits the Christiansen effect (described in detail in ref. [7]) to visualize the isotherms in the liquid phase in a thin packed bed cooled from above, but the information on the solidification front is again two-dimensional. It is clear that an imaging technique, such as Magnetic Resonance Imaging (MRI), based on radiation more penetrative than visible light is a natural candidate for porous media diagnostics, cf. Bories et al. [7], Shattuck et al. [8], Georgiadis [9], and Shattuck et al.[10].

We are focusing here on the case of freezing in a cylindrical container filled with unconsolidated packed beds and cooled from below. The objectives of the present work are: (1) to examine the new challenges that the MRI experimentalist faces when probing freezing of interstitial water, and (2) to study the effect of packed bed coarseness on ice production and front morphology by considering two different packings in the same container. The outline of this document is as follows: In section 2, the working principles of MRI are described, along with estimates on spatial resolution and collateral heating. Section 3 gives the details of experimental setup and experimental protocol. In section 4, the experimental results

(qualitative and quantitative) are reported, and comparisons are made with a simple model for solidification. Finally, in section 5, conclusions and a listing of the limitations of MRI are given.

2. MAGNETIC RESONANCE IMAGING (MRI)

In complex multiphase systems there are obvious limitations with imaging systems employing visible light. Unlike X ray imaging, Magnetic Resonance Imaging (MRI) does not depend simply on electromagnetic radiation beam attenuation through the sample but rather on the selective interaction of Radio Frequency (RF) photons with nuclei. Therefore, absorption is proportional to the number of nuclei per unit volume, or spin density. However, the principal factor determining the contrast of the MRI signal is not the spatial variation of nuclear density, but the highly heterogeneous distribution of the nuclear spin-relaxation rates in the sample.

MRI can be used to probe liquids whose constituent molecules have unpaired nuclear spins, such as the hydrogen (H^1) nucleus (proton) of water, cf. Ernst et al. [11]. The spins resonate at a frequency which is proportional to the local strength of an externally imposed magnetic field, $\omega_0=\gamma B_0$. In the following, the exposition proceeds with the imaging method and RF pulse sequence employed, and finally available MRI hardware and experimental procedure. This is needed in order to appreciate the constraints that the MRI operator has to operate under. For completeness, a short list of scan (operator controlled) and intrinsic (sample dependent) parameters in a standard MRI method (multi-slice 2-D Fourier Transform with spin echo) is given in Table 1, following Wehrli et al. [12] and Perlin and Kanal [13].

Three-dimensional imaging (say in x-y-z coordinates) is accomplished by using magnetic field *gradients* to disperse the resonating frequencies in the field of view. The switching of the gradients is coordinated with the RF pulse sequence chosen. A standard 2D MRI procedure, *spin warp*, employing the *spin echo* sequence, involves repetition of the following steps [9]:

(1) The spins in a slice of water normal to the z-axis are synchronized by applying a frequency-selective circularly-polarized RF pulse in the presence of a magnetic z-gradient. The excited slice location and thickness (THICK) depends on the imposed magnetic field and the bandwidth of the RF pulse (recall: $\omega=\gamma B$ everywhere).

(2) A magnetic y-gradient applied during a fixed time interval causes spins to acquire phase angle differences according to their y-position *(phase encoding* during excitation).

(3) x-encoding and *readout* (detection) is performed as follows. The RF coil records the spin signal in the presence of a magnetic field gradient along x. The spins resonate at frequencies determined by their x coordinate. The Fourier transform of this signal yields the number of spins with a given frequency, and thus the distribution of the spin density, ρ , along x. During the readout period (less than 10 milliseconds) the signal is digitized into NF discrete samples.

The above sequence is repeated NP times by systematically varying the magnitude of the y-gradient in step (2). The period between repetitions, TR, cannot by much shorter than a sample-dependent relaxation time T1, which is about 1 sec for water. It is possible to utilize the time following sampling by

sequentially exciting several other z-slices at a given value of the phase-encoding gradient. This sequential excitation of adjacent slices can be repeated until the nuclei in the first slice have relaxed sufficiently (T1 relaxation) to be exposed to another value of the phase-encoding gradient and be re-excited by another RF pulse. This method, represented in Figure 1, is termed *multi-section* or *interleaved multislice* imaging. Figure 1 presents the RF excitation pulse and the RF detected pulse. Interleaving in this fashion not only lowers the scan time per slice ten- to twenty-fold, but also makes any temporal instabilities (over times longer than TR) equal for all slices.

The distribution of water in the whole z-slice is obtained in terms of a pixelated image. The intensity at pixel is proportional to water concentration (averaged over the slice thickness) at the corresponding x-y coordinate. The absolute signal intensity is proportional to the number of spins that are excited in each voxel (volume element), which scales with the elementary volume (FOV/NF)X(FOV/NP)X(THICK). For the spin echo pulse sequence, the relative signal intensity scales with ρ [1-exp{-TR/T1}] exp{-TE/T2}. Consequently, the contrast between two different phases of water with comparable T1 values, such as liquid water (subscript L) and ice (subscript S), varies as

$$1\text{-}\exp\{-TE/T2_S + TE/T2_L\}.$$

Typically $T2_S$=25 μsec to 2 msec and $T2_L$=50 msec ($T2_S << T2_L$), so there is strong contrast at the liquid water-ice interface, with a significant drop in intensity in the ice regime. On the other hand there is no MRI signal from materials without chemically identifiable protons (ρ=0). Nevertheless, signal is received from all molecules in the field of view containing hydrogen, but this signal can be differentiated (in frequency space) from that emitted from the -OH group of the liquid water since the hydrogen is bound to different chemical groups. In the case of ethyl glycol (which is used as a coolant in our experiments), for example, signal is received from the ethyl protons but this leads to a 310 Hz Larmor frequency shift from that corresponding the -OH group.

In order to increase the signal-to-noise ratio, the whole experiment is also repeated NEX times and the results averaged. The number of the total repetitions then becomes (NP)X(NEX) which implies that the signal-to-noise ratio is also proportional to $\{(NP)X(NEX)\}^{1/2}$. Finally, the total scan time required is

$$Ttot=(NEX)X(NP)X(TR). \quad (1)$$

This is equivalent to approximately four minutes in our experiments. During this time, the test section is bathed in a static magnetic field B_0, time-varying gradient magnetic fields, and RF radiation from the sender-receiver coil. Only the RF contribution constitutes a significant thermal power input to the test section for the parameter range we employed, cf. Schaefer [14]. Starting with a quasi-static model for electromagnetic interaction between a coil with a uniform RF field and an insulated sphere of stagnant liquid water (approximating our test section), we arrive at an estimated temperature rise of only $\Delta T=0.0027\ ^0C$. The formula employed in this calculation is [14]

$$\Delta T = SAR\,\frac{Ttot}{C_L} \qquad \text{with} \quad SAR = \frac{\sigma\,\omega_0^2\,B_1^2\,R^2}{20\rho}\left(NEX \times NP \times NSLICE\,\frac{TRF}{Ttot}\right) \tag{2}$$

where SAR is the average specific absorption rate (absorbed RF power per unit of mass), σ = 1 Siemens/m (a rather high estimate of the electrical conductivity of the sample), B_1 is the magnitude of circularly-polarized magnetic field corresponding to the RF pulse, R is the radius of the hypothetical sample sphere, and TRF the individual RF pulse duration. B_1 depends on the shape of the RF pulse and is inversely proportional to TRF. We assumed sinc-modulated 90^0 and 180^0 pulses in our use of (2) and the MRI parameters used in the scanning of fine packed beds given in Table 1. The quantity in parenthesis represents the "duty cycle" of the MRI sequence, that is, the percentage of time when the RF coil transmits.

In the case of imaging immobile water in the pore space with a typical set of MRI parameters (given in Table 1), there are two main factors that could limit the spatial resolution below the value implied by the pixel number and the FOV. They are both related to the presence of interfaces. Owing to the creation of local magnetic susceptibility gradients, air-water interfaces generate distorted images, cf. Bakker et al.[15]. During our experiments we tried to eliminate all air bubbles from the area of interest. To prevent other susceptibility mismatch areas, we opted for materials of comparable magnetic properties. Solid-water interfaces on the other hand are sites of constrained water molecules (bound water) which results in reduced T2 times. This can be translated to *linewidth-broadening* in terms of an uncertainty, Δfreq, in the frequency domain, which is inversely proportional to T2. The spatial uncertainty, or limit of resolution, in the direction of an applied magnetic gradient, Grad, becomes: $2\,\pi\,\Delta\text{freq}\,(\gamma\,\text{Grad})^{-1}$. We have observed Δfreq in the range of 40 Hz for liquid water-filled packed beds constructed of glass beads. Using the typical value of Grad=1.5 Gauss/cm (1.5×10^{-4} Tesla/cm), we arrive at a resolution estimate of 0.39 mm. Direct imaging of ice-air interface with MRI presents a challenging problem: in addition to the loss of signal described in the previous paragraph, spatial resolution decreases by an order of magnitude. Using a linewidth of Δfreq=400 Hz (measured by Mizuno and Hanafusa [16]), the theoretical resolution at the ice-air interface becomes 3.9 mm.

3. MRI SCANNER AND TEST SECTION

The MRI experiments were performed on a B_0=4.7 Tesla ($\omega_0=2\pi \times 200$ rad sec^{-1}) SISCO system located at the Biomedical Magnetic Resonance Laboratory of the University of Illinois at Urbana-Champaign. The superconducting magnet (which imposes the static B_0 field) forms a horizontal bore enclosing resistive shim coils (to adjust the magnetic field inhomogeneities) and magnetic gradient coils. The free bore size (space available for our test section) is ultimately constrained by the internal dimensions of the RF excitation/readout coil. We used a saddle-type coil with 16.12 cm available bore diameter.

An MRI experiment starts with a set-up protocol (which involves some operator-intensive trial and error procedures). Here are the basic steps (also refer to Figure 2):

(1) Secure the test section (sample) at the center of the magnet inside the RF coil.
(2) Tune the coil-sample system. The objective is to minimize the reflected RF power by adjusting the matching and tuning capacitors connected to the coil.
(3) Shim the magnet (increase the homogeneity of the magnetic field inside the coil) by electronically adjusting the shimming coils.
(4) Determine the RF transmitter power level. This determines RF power settings for 90^0 and 180^0 pulse, required for the spin-warp procedure.
(5) Set the appropriate FOV, slice orientation, TR, TE, etc.

The operator can then run a plethora of imaging experiments by using various macros from the workstation which drives the scanner. The images are typically first displayed (during acquisition) on the control console, then saved and finally pre-processed with the software package VIEWIT (developed in the Biomedical Magnetic Resonance Laboratory of the University of Illinois at Urbana-Champaign) before downloading them to the image analysis computers.

The MRI test section contains a heat exchanger that was designed to operate within the specifications required to freeze water inside the bore of the scanner (Figure 2). Owing to the presence of strong magnetic fields and RF radiation in MRI, ferromagnetic materials cannot be placed in or near the bore of the scanner. Therefore, the heat exchanger was constructed almost entirely of plastics, with the exception of the heat exchanger surface which is composed of aluminum nitride, a ceramic. Aluminum nitride has the advantage of relatively high thermal conductivity (one third of that of copper), poor electrical conductivity (which minimizes RF power absorption), and similar magnetic susceptibility to the rest of the test section. The cooling fluid, a mixture of ethylene glycol and water, is provided by a Neslab RTE-210 recirculating bath. The use of ethylene glycol requires that the materials used in the heat exchanger are resistant to chemical corrosion. The lower half of the test section (the shell housing the cooling fluid) is connected through 10 m of insulated Tygon^{TM} tubing to the bath, so that the distance between the bath and the magnet is approximately 5 m, which brings the susceptible bath parts (pump, electronics) within the 10 to 20 Gauss range. For comparison, the earth's magnetic field is equal to 0.5 Gauss.

The shell of the test section is constructed of natural Delrin^{TM}. Delrin was selected for its good magnetic properties, corrosion resistance, and ease of machinability. The outer dimensions of the test section are restricted by the inner diameter of the imaging RF coil (refer to Figure 2). There are two chambers in the test section. Cooling fluid from the bath circulates in the lower chamber. The upper chamber is a cylindrical cavity with 12.7 mm thick walls, with inner dimensions of H=40.26 mm (height) and D=76.2 mm (diameter), and a chimney-like hole on top for venting and allowing the water to escape during freezing. It houses the sample: a solid matrix consisting of a packed bed of glass beads fully-

saturated with water. The two chambers are divided by a circular disk of 108 mm-diameter aluminum nitride which acts as the heat exchange surface between the ethylene glycol and the sample. The thickness of the aluminum nitride plate is 1 mm (0.040 inch). This thickness allows rapid heat exchange between the two chambers while maintaining enough structural integrity to prevent failure of the plate due to pressure differential between the upper and lower chambers. Two nitrile O-rings, one on each side of the aluminum nitride plate, form the seal that prevents leakage from either chamber. An extra O-ring is fitted directly between the two pieces of delrin to prevent fluid escaping to the surroundings in case either of the interior O-rings fail. The upper chamber contains three nylon plugs, which can be fitted with thermal probes to monitor the temperature in the upper chamber. During the coarse-packing experiment discussed below, a thermocouple was attached on the aluminum nitride plate, on the side of the packed bed, and the temperature was monitored when the MRI scanning was off. Finally, the whole test section is thermally insulated by enclosing it in a jacket made from a 2 cm thick sheet of insulation.

4. EXPERIMENTAL RESULTS AND DISCUSSION

Experimental Protocol and Pore Space Reconstruction

MRI can capture the phenomenon of freezing in a fully saturated porous medium by allowing the visualization of progressive stages of the liquid-solid interface. In our experiments, only liquid water gives significant MRI signal because the relaxation time T2 of ice is very short (see discussion in Section 2). The test section was positioned in the scanner so that the cold plate was horizontal and the sample was cooled from below. The upper chamber was filled with uniform glass beads and completely saturated with deaerated water. Two sets of packed beds were used: a coarse-packing with d=14 mm beads, and a fine-packing with d = 3 mm beads. For the coarse packing, MRI acquisition was performed in a series of transient experiments in which the bath and the plate were left to reach thermal equilibrium at -1^0C, and then the bath thermostat was set to a low temperature. The plate would then cool down slowly (owing to the large thermal mass of the coolant in the bath and the 10 m of tubing). Figure 3 gives the transient behavior of the bath temperature and the temperature at the aluminum nitride plate surface (packed bed side) as measured with a thermocouple, as well as the average height of ice in the test section obtained via image processing the MRI scans. The jump in the plate temperature at t=0 marks the onset of freezing. This temperature variation is typical of such phenomena, cf. Figure 2 of Yang et al. (1993). For the fine packing, the test section was imaged as it cooled down starting from 22^0C (room temperature).

The first coarse-packing experiment consisted of six consecutive MRI scans. Each scan produced a set of twelve 2-D horizontal slices normal to the vertical axis of the test section, which corresponds to the vertical axis y of Figure 2. The slices are positioned 0.5 cm apart to span the entire inner volume of the upper chamber which contains the packed bed. The image of each slice contains 256 by 128 pixels, corresponding to a field of view of 10 by 10 cm. The visualization of the 3D matrix of packed beads

contained in the MRI test section, before the onset of freezing, was used to assess the accuracy of the MRI data in recreating volumes. First, the beads' cross sections were created by digitally enhancing the glass-water interface in the MRI slices and the whole packed bed was reconstructed as a 3D object by interpolating between the slices. Second, the pore space was directly measured by emptying the test section, counting the beads, and computing their volume. Comparison between the MRI-measured (ϕ=0.50) and the directly-measured (ϕ=0.49) pore space volumes gives a 2% volumetric error. There was no appreciable distortion (deviation from sphericity) for the beads in this level of resolution. The packed bed was also visually reconstructed by rendering the bead surfaces and finally projecting it at 30^0 and 20^0 tilts. Figure 4 gives these two views of the packed bed. Fusion of the two views in the brain yields the illusion of stereoscopic view of the object.

The porosity of the fine-packing bed (ϕ=0.42) was estimated by weighing a known quantity of the 3mm beads, then weighing the whole sample contained in the cavity, estimating the total quantity and computing its volume (since we have monodisperse spherical beads), and finally subtracting from the known cavity volume. In our modeling below, we use ϕ=0.49 for the coarse and ϕ=0.40 for the fine-packing beds.

As is obvious from Figure 3, each MRI scan obtained with the multislice sequence coincides with approximately $\Delta T = 1.5^0C$ temperature increase in both bath and aluminum nitride plate (measured immediately after each scan) for the coarse-packing, and up to $\Delta T = 2^0C$ for the fine packing. Is this caused by RF thermal input ? The a-priori estimate of equation (2) in Section 2 was only 0.0027 ^{0}C. This estimate can be checked against an upper limit obtained on the basis of the RF transmitter power (applied to the RF coil and adjusted by the operator to produce the 90^0 and 180^0 pulses). Indeed, the delivered energy during the Ttot=341 sec of the NSLICE=9 fine-packing experiment was 24.12 Joules. This implies that the temperature of a water sphere of radius 0.038 m would be raised by 0.015 ^{0}C at most. This is consistent with the a-priori estimate because not all power applied to the RF coil is absorbed by the sample. So, it is certain that RF heating did not cause the 1.5-2^0C temperature rise. Evidence of spurious fluctuations of the cooling bath thermostat indicator during the MRI scanning points out that electromagnetic influence of the scanner was severe enough to relax the temperature control of the bath. These inteferences occured only during scanning, and the bath thermostat returned to the preset value immediately after each scan.

Ice Front Reconstruction in Coarse-Packing Bed

The liquid water-saturated pore space has been volumetrically recreated from one scan during freezing and is given in Figure 5(a). The top is truncated above a horizontal slice in order to visualize the spherical cavities corresponding to the spherical beads (glass beads are not visible in MRI). Similar cavities are also distributed in the interior of the truncated cylindrical volume (as the cut-out in Figure 5(a) demonstrates). The prominent trench visible on the top marks the presence of an air bubble which is trapped under the upper wall of the cavity. During subsequent experiments, care was taken to eliminate

such bubbles by tilting and shaking the sample, and verifying via MRI the absence of such odd-shaped cavities.

The second coarse-packing experiment, the results of which are presented in Figure 3 and will be further discussed below, was composed of six MRI scans. Each scan corresponds to a set of twelve 2-D vertical slices, each slice positioned normal to the z axis of Figure 2. The slices are 0.5 cm apart, creating a 6 cm-thick stack, and again have 256 by 128 pixel resolution. This experiment involves vertical sectioning (normal to the front) which allows increased resolution of the solidification front, and permits the reconstruction of the solid-liquid interface as a function of time and space. Each scan required approximately 4 minutes. The position of the freezing interface in the central slice (section containing the vertical axis of the cylinder) is given in Figure 5(b). The general shape of the interface becomes increasingly convex as the front evolves upwards.

Using the total data set (12 slices), the volume of ice (including the glass beads it encloses) is estimated. The average height of the frozen column, which is bounded by the aluminum nitride plate from below and by the water-ice front from above, is computed by integrating the MRI slices and is given in Figure 3. Based on the measured front speed, the ice interface moves an average 1.6 mm during each 4 min MRI scan. This is commensurate with the a-priori estimate of 0.39 mm resolution at the ice-glass interface (based on linewidth-broadening) and a pixel resolution in the range of 0.39-0.156 mm (based on the field of view given in Table 1).

Ice Front Reconstruction in Fine-Packing Bed

The progression of the ice-water interface in the d=3mm packed bed is similarly tracked with MRI. Figure 3 depicts the average interface height as a function of time, starting from t=0 when the onset of freezing was estimated to have occurred, superposed on the bath temperature record. Contrary to the previous experiments, a variable number of vertical slices was acquired during each MRI scan, each resulting to a different temperature rise. The first two data points were acquired with a single slice scan, the fourth with NSLICE=5, and the third and fifth with NSLICE=9. Figure 6(a) gives the time evolution of the solid-liquid interface during freezing, by superposing the slice containing the vertical axis of the cavity. It is clear that the ice-water interface remains much flatter than the coarse-packing case. During the last scan, a water-filled cavity appeared near the left boundary, probably caused by the local remelting of ice, and by the shifting of the beads and the creation of a lens-like pore in that area. After the last scan represented in Figure 3, the bath temperature was raised above freezing, and the ice layer was thawed from below as the aluminum nitride plate was heated. A qualitative view of the remelting is presented in Figure 6(b), where the location of the lower water-ice interface is marked. That interface is convex signifying the presence of recirculation in the underlying liquid water during melting. The modification of the shape of the lens-like pore as the melting progresses does not mean that the pore closes, as the presented views correspond to different slices of the sample.

One-Dimensional Model for Ice Front Propagation

The upwards movement of the ice-water interface during freezing was simulated with an one-dimensional conduction model assuming that the water saturated packed bed is a homogeneous medium in contact with an isothermal cold plate from below and unbounded from above. It is assumed that the packed bed-water system is stably stratified and conduction is the dominant heat transfer mechanism. The fine-packing bed experiment was simulated with T_i-T_F=22^{0}C superheat (difference between packed bed temperature and freezing point) and T_F-T_C=8^{0}C, in contrast to the T_i-T_F=-1^{0}C supercool and T_F-T_C=5^{0}C for the coarse-packing case. The thermal properties of the solid matrix-liquid water and solid matrix-ice portions of the sample were estimated by volumetrically averaging the properties of the constituents, starting from the properties given in Table 2. For example, the effective conductivity of the frozen and unfrozen portions were estimated by the following formulas

$$\kappa_{SM} = \phi\kappa_S + (1-\phi)\kappa_{Glass}, \qquad \kappa_{LM} = \phi\kappa_L + (1-\phi)\kappa_{Glass} \tag{3}$$

The solution of this freezing front propagation problem (a variation of the Stefan problem) is given in Poulikakos [17] in terms of a nonlinear algebraic equation for a properly scaled distance between the front and the cold plate, which is defined as 0.5 z $(\alpha_{SM}\, t)^{-1/2}$. The solution of this equation was obtained for two porosities for each of the experiments: ϕ=0.49 and ϕ=1 (coarse-packing) and ϕ=0.40 and ϕ=1 (fine-packing). The results for ϕ=1 correspond to the freezing of pure water and are used as a control. The results are presented in Figure 7, in terms of a non-dimensional front height z* versus a non-dimensional time

$$\tau = \left[\frac{a_L}{H^2} \frac{(T_F - T_C)}{L} C_L \right] t \tag{4}$$

This non-dimensional time is defined slightly different in Yang et al. [5].

Due to the non-uniformity of random packing of the spheres near walls, the porosity is very high in a 2 d to 3 d thick annular region near flat walls compared to the bulk value at the core (near the vertical axis of the cylindrical cavity). The simulation results depicted in Figure 7 indicate that the growth of the ϕ=0.49 and ϕ=0.4 fronts (representing the core) is higher than that of ϕ=1 (representing the wall region). This is consistent with the convexity of the observed freezing front depicted in Figure 5(b). Solidification in the core proceeds faster than at the perimeter. This "wall-effect", which is extremely pronounced in the coarse-packing bed (D/d=6), affects the solidification front in the following ways: The conductivity of glass is approximately twice that of water, see Table 2. The increased thermal conductivity of the packed bed is therefore higher at the core (near the vertical axis of the cylindrical cavity) than the perimeter. Hence, the core region cools earlier. More latent heat is released (during freezing) near the walls since there is more water there. This effect is insignificant for the fine-packing bed (D/d=25), and again the MRI observation confirm this, cf. Figure 6(a).

The solution of the Stefan problem with isothermal cooling plate yields z* proportional to $\tau^{0.5}$. The model predictions do not reproduce quantitative the observed front growth rates. Our experimental results were correlated by the following power laws:

$$z^*_{fine} = 4.37 \quad \tau^{0.62}, \qquad z^*_{coarse} = 5.84 \quad \tau^{0.71} \tag{4}$$

The disagreement can be attributed to the exclusion of two- and three-dimensional effects, and the adoption of a simplified thermal boundary condition. Among the two model deficiencies, the latter is significantly more severe. It is clear from Figure 3 that the bottom plate did not remain isothermal during the freezing. Given the fact that the plate was convectively cooled by a thermostatically controlled bath, a convective boundary condition at the cooled wall is more appropriate. The approximate solution of Ma and Wang [18] implies that, for negligible superheat (the coarse bed experiment), the front progresses as $z^*=c_1 \tau - c_2 \tau^2 +$ ..., where c_1,c_2 are constants that depend on the heat transfer coefficient between the plate and the cooling fluid. This is consistent with the measured exponent 0.71 of equation (4), as well as the linear growth of the front during the first three scans for the coarse bed given in Figure 7. The temporal behavior of the freezing front with significant superheat (fine-packing bed experiments) is more complicated. The front growth rate is slower than that for the zero superheat case, it reaches a peak value, and then decays [18]. This might account for the change of slope of the z* versus τ curve given in Figure 7. Finally, it is worth noting that the fine-packing bed result given in (4) agrees with the exponent 0.62 measured by Yang et al. [5], obtained with a corresponding D/d=10 and similar superheat.

Recommendations for Improved Methodology

It is clear that the temperature rise experienced by the sample during MRI imaging is an unwanted byproduct of the scanner-bath interaction, so it is important to examine whether the thermal power input has affected directly the freezing process. Since $C_L \Delta T << L$, the thermal input is much less that the latent heat released during freezing (and transported away via the cooling bath). Shortening the scan time will bring a commensurate reduction of interference (and heating), but this requires the decrease of resolution in terms of pixel size (NP factor) or 3-D imaging (NSLICE factor). Indeed, no significant temperature rise was recorded during the early scans (NSLICE=1) for the fine-packing case depicted in Figure 3. Rather that decrease the scan time, we are making efforts to eliminate the electromagnetic coupling between the bath and the scanner. One practical solution is to cool the test section with liquid nitrogen.

Increasing the spatial resolution will incur penalties in terms of longer scanning times, as the analysis in Section 2 implies. This will limit the temporal resolution which is critical in imaging evolving solidification fronts. It is worth mentioning in passing that the success of the employed MRI sequence in our experiment hinges on the fact that motion in the interstitial water during freezing was negligible. Figure 6(a) gives an example of the generation of motion artifacts in the water-ethylene glycol mixture reservoir.

Improved MRI sequences are necessary to compensate for flow in the field of view and to quantify the velocity field, cf. Shattuck et al. [10].

In order to improve the modeling of freezing front propagation in complex media, the pioneering work of Hong et al. [2] shows that it is feasible to couple MRI results with numerical heat transfer simulations. The freezing front boundary obtained by MRI sectioning can be used as a boundary condition for a numerical scheme (a finite-difference scheme was used in [2]) to produce the temperature field throughout the sample. The slow speed of propagation (in our experiments, Ste=0.0625 for coarse and Ste=0.123 for fine-packing) reduces the heat transfer model to a quasi-steady conduction equation, which can be solved on a grid that is commensurate with the pixelated MRI field of view. This is particularly useful in the frozen domain which is not resolved in MRI.

5. CONCLUSIONS

A novel application of a non-invasive high-resolution imaging technology, Magnetic Resonance Imaging (MRI), in the study of structure evolution in two-phase media of ice-water interfaces has been demonstrated. MRI relies on the interaction of radiofrequency radiation and nuclear spins, in the presence of magnetic fields. We have used a multislice MRI sequence to map the freezing of water contained in a coarse and a fine packed bed cooled from below. The position of the ice interface was visualized, indirectly, by mapping the water column in space and time. The average distance of the interface from the plate was used to quantify the solidification rate. Initially, solidification was found to progress linearly with respect to time in the case with negligible superheat, and faster than the square root of time in later stages. The shape of the solidification front became convex upwards during freezing in the coarse-packing bed (D/d=6) owing to the wall effect, while the front inside the fine bed (D/d=25) remained flat. A summary of the constraints of MRI, in its present implementation, is given below.

Non-ferromagnetic media with low electrical conductivity are required for the sample, and magnetic susceptibility interface artifacts can be severe, especially near gas interfaces. What MRI lacks in theoretical resolution (10 μm-wide pixels, without special RF coils, compared to 1 μm for optical methods), it makes up in penetration depth into opaque media. In our experiments, the 390-156 μm pixels provide adequate resolution in space, and allow the reconstruction of the freezing front in time. Finally, in order to produce quantitative 3D reconstruction, MRI studies rely on extensive image processing and image analysis. Acquiring and analyzing 3D data (representing complex morphologies) makes high demands in terms of gigabyte-size digital storage, high resolution color displays, or video. The MRI technique has seen explosive growth in the field of biomedical imaging during the last ten years, and has come full cycle back to the applied sciences. This work serves to demonstrate that the MRI user has to be familiar with the fundamental as well the applied aspects of this very promising non-invasive tool before adopting it in a specific application.

ACKNOWLEDGMENTS

We would like to thank Mr. Paul Greywall for his assistance in constructing the test section, and during acquisition and image processing of some preliminary results. We gratefully acknowledge the financial support of the Department of Mechanical & Industrial Engineering, the Research Board, and the Air Conditioning & Refrigeration Center (Dr. Clark Bullard, director) of the University of Illinois at Urbana-Champaign, the National Science Foundation (grant CTS-9396252), and the Electric Power Research Institute (grant WO8034-07, Dr. Sekhar Kondepudi, monitor). Special thanks to Dr. Doug Morris and to Dr. Andrew Webb of the Biomedical Magnetic Resonance Laboratory of the University of Illinois at Urbana-Champaign (Dr. Paul Lauterbur, director).

REFERENCES

1. L.D. Hall and T.A. Carpenter, Magnetic Resonance Imaging: A New Window into Industrial Processing, *Magnetic Reson. Imag.* **10**, 713-721 (1992).
2. J.S. Hong, S. Wong, G. Pease, and B. Rubinsky, MR Imaging Assisted Temperature Calculations During Cryosurgery, *Magnetic Reson. Imag.* **12**(7), 1021-31 (1994).
3. J.A. Weaver and R. Viskanta, Freezing of liquid-saturated porous media, *ASME J. Heat Transfer* **108**, 654-659 (1986)
4. Chellaiah S. and Viskanta, R. (1989), Freezing of water-saturated porous media in the presence of natural convection: experiments and analysis, *ASME J. Heat Transfer* **111**, 425-432.
5. C-H. Yang , S.K. Rastogi, and D. Poulikakos, Freezing of water-saturated inclined packed bed of beads, *Int. J. Heat Mass Transfer* **36**(14), 3583-3592 (1993).
6. Lein H. and Tankin R.S. (1992), Natural Convection in porous media-II. Freezing, *Int. J. Heat Mass Transfer* **35**(1), 187-194.
7. S.A. Bories, M.C. Charrier-Mojtabi, D. Houi, and P.G. Raynaud, Non Invasive Measurement Techniques in Porous Media, in *Convective Heat and Mass Transfer in Porous Media*, S. Kakaç et al (eds), Kluwer, Netherlands, NATO ASI Vol E **196**, 883-921, (1991).
8. M.D. Shattuck, R.P. Behringer, J.G. Georgiadis, and G.A. Johnson, Magnetic Resonance Imaging of Interstitial Velocity Distributions in Porous Media, in *Experimental Techniques in Multiphase Flows*, TJ O'Hern & RA Gore (eds), ASME, New York, FED-Vol **125**, 39-46 (1991).
9. J.G. Georgiadis, Multiphase Flow Quantitative Visualization, *Applied Mechanics Review,* **47**(6), part 2, S315-S319 (1994).
10. M.D. Shattuck, R.P. Behringer, G.A. Johnson, and J.G. Georgiadis, Onset and Stability of Convection in Porous Media: Visualization by Magnetic Resonance Imaging, *Physical Review Letters* **75**(10), 1934-1937 (1995).

11. Ernst R.R., Bodenhausen G., and Wokaum A. (1987), *Principles of Nuclear Magnetic Resonance in One and Two Dimensions*, Clarendon, New York, Chap 10.
12. F.W. Wehrli, J.R. MacFall, D. Shutts, G.H. Glover, N. Grigsby, V. Haughton, and J. Johanson, The Dependence of Nuclear Magnetic Resonance (NMR) Image Contrast on Intrinsic and Pulse Sequence Timing Parameters, *Magnetic Resonance Imaging* **2**(1), 35-243 (1984).
13. M. Perlin and E. Kanal (1989), Goal Directed Magnetic Resonance Imaging: Clinical Practice and Computer Implementation, in *Advances in Magnetic Resonance Imaging,* E. Feig (ed), Ablex Publishing, Norwood NJ, Vol **1**, 183-224.
14. D. J. Schaefer, Bioeffects of MRI and Patient Safety, *The Physics of MRI: 1992 AAPM Summer School Proceedings* , 607-646. Medical Physics Monograph No. 21, American Institute of Physics (1992).
15. C.J.G. Bakker, R. Bhagwandien, M.A. Moerland, and M. Fuderer, Susceptibility Artifacts in 2DFT Spin-Echo and Gradient-Echo Imaging: the Cylinder Model Revisited, *Magnetic Reson. Imag.* **11**, 539-548 (1993).
16. Y. Mizuno and N. Hanafusa, Studies of Surface Properties of Ice Using Nuclear Magnetic Resonance, *J. Physique* **48**(3), C1-511 -- C-517 (1987).
17. D. Poulikakos (1994), *Conduction Heat Transfer*, Prentice-Hall, New Jersey, Chapter 9.
18. J. Ma and B-X. Wang, The penetration rate of solid-liquid phase-change heat transfer interface with different kinds of boundary conditions, *Int. J. Heat Mass Transfer* **38**(11), 2135-2138 (1995).

Table 1.

List of operator-controlled) and intrinsic parameters in a standard MRI method (multi-slice 2-D Fourier Transform with spin echo). The values in parenthesis correspond to the actual values used in the freezing experiments in coarse-packing (first value) and fine packing (second value) bed.

MRI scan parameters

FOV = field of view, length or width size of the image (10 cm, 8 cm).

NP = number of phase-encoding gradients employed in the spin-warp sequence (128, 256). One coordinate of the 2-D Fourier transform k-space.

NF = number of frequency-encoding gradients, the other k-space coordinate (256, 512).

NEX = number of repetitions (excitations) of entire experiment for signal averaging (2, 1).

NSLICE = number of slices, each of thickness "THICK", obtained in multi-slice imaging (12, 9).

TE = echo-time between 90^o pulse and the peak spin-echo signal (0.02 sec, 0.03 sec).

TR = repetition time between 90^o RF pulses (1 sec, 1.33 sec).

Intrinsic parameters

γ = gyromagnetic ratio, 2π X42.57X10^6 rad sec^{-1} $Tesla^{-1}$ for hydrogen (H^1).

T1 = longitudinal (spin-lattice) relaxation time.

T2 = transverse (spin-spin) relaxation time.

ρ = proton spin density, number of spins per unit volume of sample.

Table 2.

Thermophysical parameters for the components of the packed bed.

	Liquid water	Ice	Borosilicate glass
density [kg m^{-3}]	1000	920	2,640
conductivity[W m^{-1} K^{-1}]	0.569	1.88	1.09
diffusivity [m^2 sec^{-1}]	1.35 x 10^{-7}	1.0 x 10^{-6}	5.1 x 10^{-7}
fusion latent heat [Jkg^{-1}]	333 x 10^3		

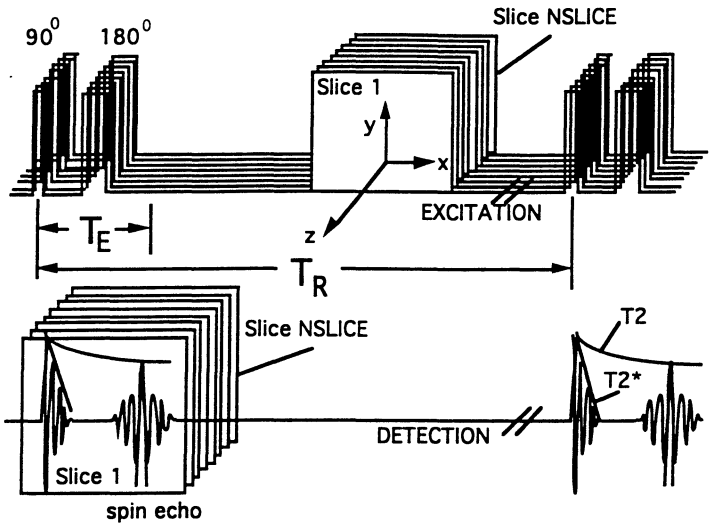

Figure 1 RF excitation and detection during multisection imaging with spin echo. The 90^0 and 180^0 excitation RF pulses are required to encode space before the spins loose coherence (relax). T2 is the spin-spin relaxation time, characteristic of loss of phase coherence in the x-y plane. The signal acquisition from a stack of NSLICE z-slices is interleaved (in Fourier-space). A single Fourier-space line (corresponding to a fixed value of the phase-encoding gradient) is acquired for each of the z-slices.

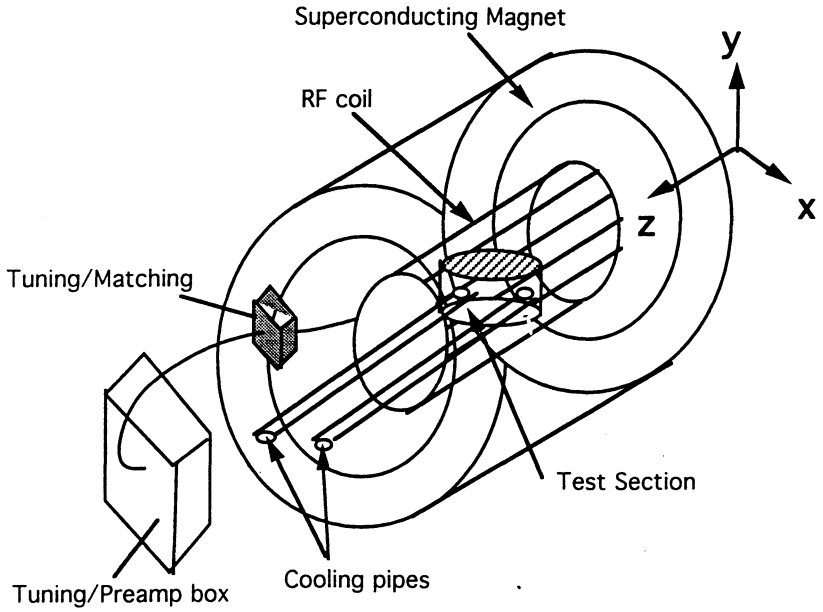

Figure 2 MRI scanner and associated hardware, all contained in a shielded room. The field of view can be anywhere inside the RF coil. The cooling pipes are connected to the bath/recirculator system, which is positioned as far from the magnet as possible in order to minimize interference. Shimming, calibration of RF power, and control of the imaging sequences, are performed from control hardware outside the MRI scanner room.

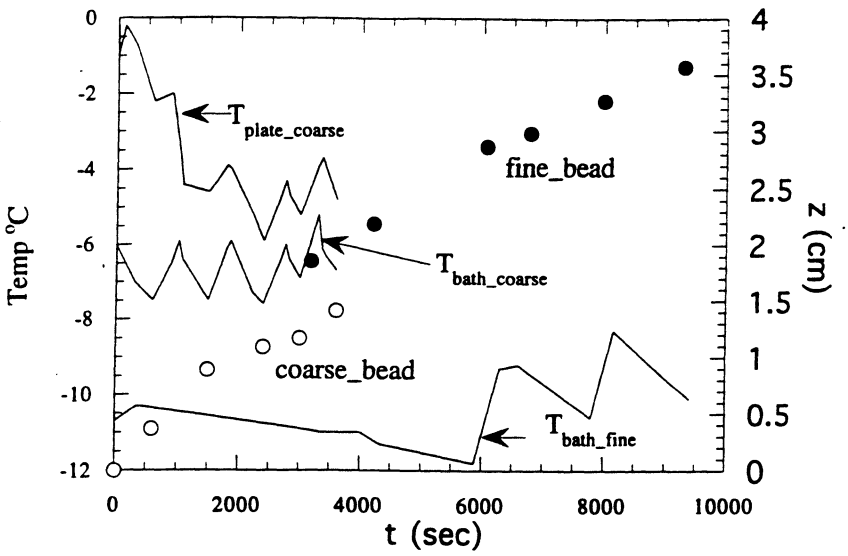

Figure 3 The evolution of average height of freezing front, cooling bath and cold plate temperature as a function of time. The jump in the coarse-packing plate temperature corresponds to the onset of freezing.

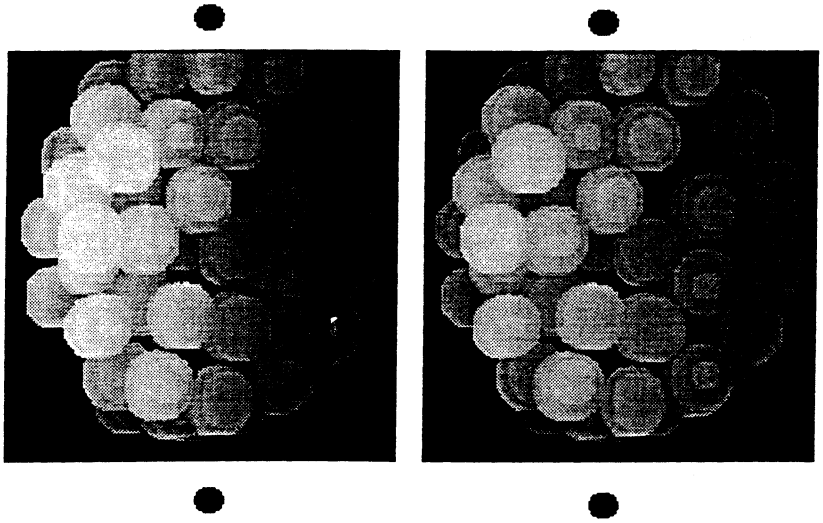

Figure 4 Stereogram of the solid matrix of the D/d=6 packed bed consisting of two simulated views of the MRI recreated object. Fusion of the two views in the brain yields the illusion of stereoscopic view of the object. The reader can achieve the stereo depth effect by holding the page at normal reading distance and relaxing the eyes (focusing at infinity) so that the dots in each pair merge.

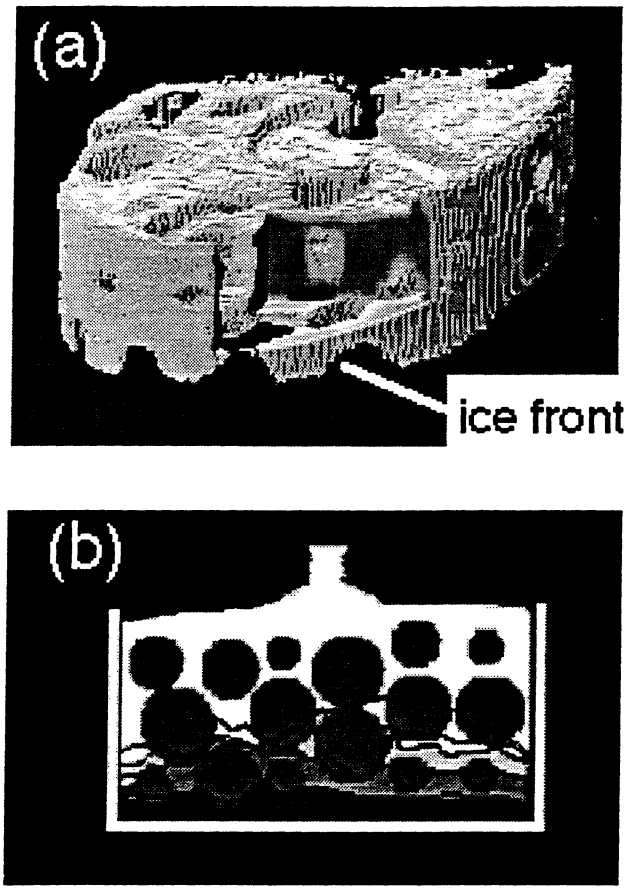

Figure 5. MRI images of freezing in coarse packed bed (D/d=6). (a) Volumetric reconstruction of the interstitial liquid water. (b) Time evolution of the liquid-solid interface. The gray disks are the cross-sections of glass beads, white denotes liquid water. Each image corresponds to the same vertical slice near the axis of the cylindrical test section. The front profiles (solid lines) are obtained at 10 min, 25 min, 40 min, 50 min, and 60 min after the freezing inception.

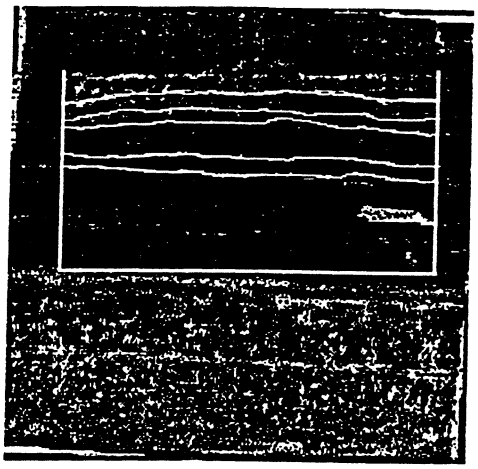

(a)

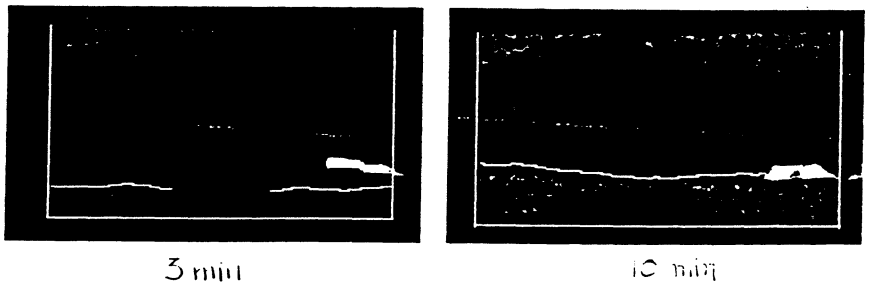

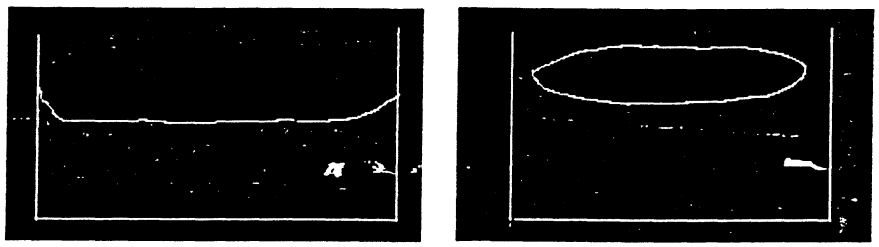

(b)

Figure 6. MRI images of freezing and thawing in fine packed bed (D/d=25). (a) Time evolution of the liquid-solid interface during freezing. Image is obtained by superimposing the central cross section. The front profiles (white lines) are obtained at 53 min, 70 min, 101 min, 113 min, 133 min, and 155 min after the freezing inception. (b) Time evolution of the liquid-solid interface during thawing.

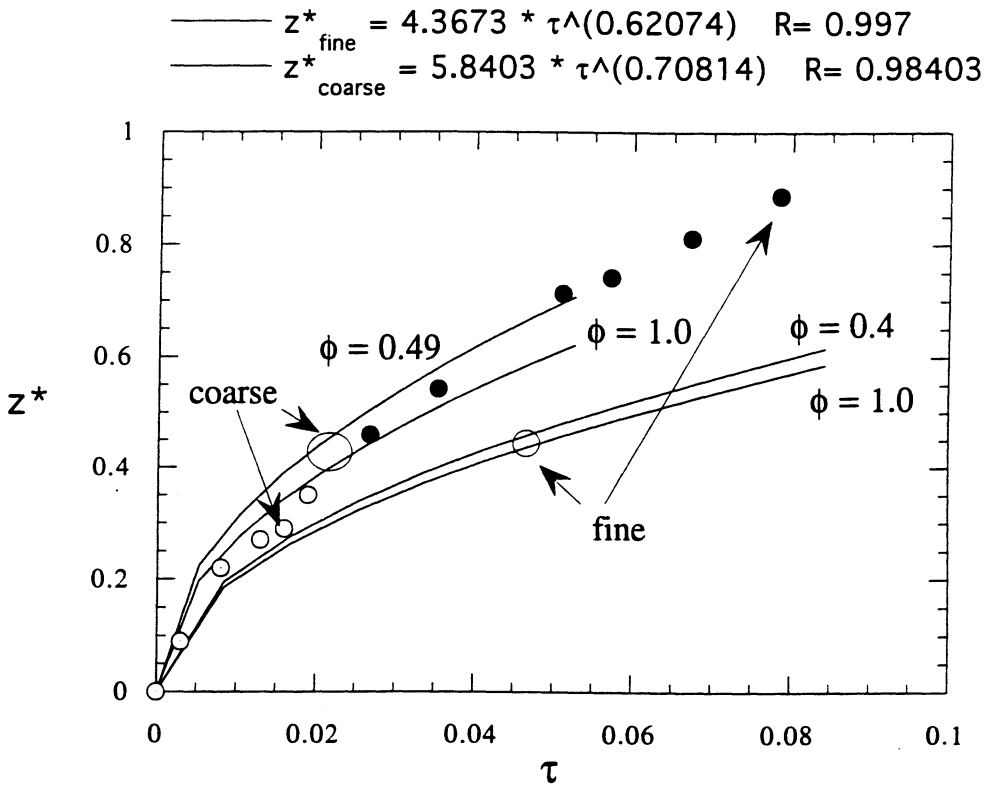

Figure 7. Comparison between measured (circles) and predicted (solid line) average front evolution as a function of time during freezing. The predictions are obtained for two porosities (bulk and wall region) for each of the two packed beds.